

# The shocked outflow in NGC 4051 – momentum-driven feedback, UFOs and warm absorbers

K.A.Pounds and A.R.King

*Department of Physics and Astronomy, University of Leicester, Leicester, LE1 7RH, UK*

Accepted ; Submitted

## ABSTRACT

An extended *XMM-Newton* observation of the Seyfert 1 galaxy NGC 4051 in 2009 revealed an unusually rich absorption spectrum with outflow velocities, in both RGS and EPIC spectra, up to  $\sim 9000 \text{ km s}^{-1}$  (Pounds and Vaughan 2011). Evidence was again seen for a fast ionised wind with velocity  $\sim 0.12c$  (Tombesi 2010, Pounds and Vaughan 2012). Detailed modelling with the XSTAR photoionisation code now confirms the general correlation of velocity and ionisation predicted by mass conservation in a Compton cooled shocked wind (King 2010). We attribute the strong column density gradient in the model to the addition of strong two-body cooling in the later stages of the flow, causing the ionisation (and velocity) to fall more quickly, and confining the lower ionisation gas to a narrower region. The column density and recombination timescale of the highly ionised flow component, seen mainly in Fe K lines, determine the primary shell thickness which, when compared with the theoretical Compton cooling length, determines a shock radius of  $\sim 10^{17} \text{ cm}$ . Variable radiative recombination continua (RRC) provide a key to scaling the lower ionisation gas, with the RRC flux then allowing a consistency check on the overall flow geometry. We conclude that the 2009 observation of NGC 4051 gives strong support to the idea that a fast, highly ionised wind, launched from the vicinity of the supermassive black hole, will lose much of its mechanical energy after shocking against the ISM at a sufficiently small radius for strong Compton cooling. However, the total flow momentum will be conserved, retaining the potential for a powerful AGN wind to support momentum-driven feedback (King 2003; 2005). We speculate that the ‘warm absorber’ components often seen in AGN spectra result from the accumulation of shocked wind and ejected ISM.

**Key words:** galaxies: active – galaxies: Seyfert: general – galaxies: feedback individual: NGC 4051 – X-ray: galaxies

## 1 INTRODUCTION

High resolution spectra of the bright Seyfert 1 galaxy NGC 4051 obtained by *Chandra*, *XMM-Newton* and *Suzaku* over the past decade have detected soft X-ray absorption lines indicating a ubiquitous outflow with velocities in the range  $\sim 200\text{--}600 \text{ km s}^{-1}$  (Collinge et al. 2001, Ogle et al. 2004, Pounds et al. 2004, Steenbrugge et al. 2009), with occasional reports of higher velocities of  $\sim 2340 \text{ km s}^{-1}$  (Collinge et al. 2001) and  $\sim 4600 \text{ km s}^{-1}$  (Steenbrugge et al. 2009). A substantially longer *XMM-Newton* observation in 2009 revealed a more complex soft X-ray absorption spectrum, with outflow velocities up to  $\sim 9000 \text{ km s}^{-1}$  (Pounds and Vaughan 2011). While rare in the soft X-ray band, similar outflow velocities are frequently observed in Fe K spectra of NGC 4051, more sensitive to highly ionised matter (Pounds et al.

2004, Lobban et al. 2012). Moreover, in an archival *XMM-Newton* search of 42 radio quiet AGN, Tombesi et al. (2010) found evidence for still higher velocity outflows ( $v \sim 0.1c$ ) in  $\sim 35\%$  of their sample, including NGC 4051. An intriguing question is whether, or how, such ultra-fast outflows (UFOs) are physically linked with the more weakly ionised and much slower outflows (‘warm absorbers’) which are also common in many bright AGN.

In an initial analysis of the 2009 *XMM-Newton* observation of NGC 4051, Pounds and Vaughan (2011; hereafter Paper I) considered an apparent correlation of outflow velocity and ionisation parameter in terms of a mass-conserved decelerating flow, perhaps resulting from strong Compton cooling after shocking of the high speed primary wind with the ISM or slower moving ejecta (King 2010; Zubovas and King 2012). A wider relevance of the shocked flow scenario

lies in the transformation of an energetic AGN wind into an outflow where the potential mechanism for galaxy feedback is the momentum thrust (King 2003, 2005).

The high sensitivity of the 2009 *XMM-Newton* observation also found several strong, blue-shifted and broad emission lines (BEL), all showing evidence of self-absorption near the line cores (Pounds and Vaughan 2011a; hereafter Paper II). Broad soft X-ray emission lines have previously been reported for NGC 4051 (Ogle et al. 2004, Steenbrugge et al. 2009), and for several other Seyfert 1 galaxies (Kaastra et al. 2002, Costantini et al. 2007, Smith et al. 2007), being interpreted by those authors as an extension of the optical/UV ‘broad line region’, envisaged as optically thick ‘clouds’ circling the central black hole. Paper II outlined an alternative origin of the broad soft X-ray emission lines in NGC 4051, arising in a limb-brightened shell of shocked gas, and noted that self-absorption in the near-orthogonal flow could explain the low velocity absorption component seen across a wide range of ionisation states.

In the present paper, we describe in Section 3 the detailed modelling of both RGS and EPIC absorption spectra using the XSTAR photoionisation code, with 5 RGS components confirming a linear correlation of outflow velocity and ionisation parameter. While low velocity/low ionisation absorption is only observed in the RGS data, the RGS and EPIC model parameters are in good agreement for the higher velocity/higher ionisation absorption. A 6th RGS component lies off the main trend, and represents the low outflow velocity observed over a wide range of ionisation. Intriguingly, a 7th RGS component has a small but significant net redshift, which we speculate might be due to shocked gas falling back towards the hole.

Section 4 uses the inter-orbit variability of Fe K absorption, reported in more detail in Paper III, to estimate the recombination time of the more highly ionised flow component (from changes in the FeXXV to FeXXVI ratio) and hence constrain the related particle density, which - with the corresponding absorption column density from XSTAR modelling - gives the thickness of the highly ionised post-shock shell. In Section 6 this value is compared with the theoretical Compton cooling length and used to derive an estimate of the shock radius.

At some point along the post-shock flow, two-body processes will become important, resulting in additional cooling (Appendix), with the flow temperature (ionisation and velocity) then falling more quickly. Section 5 examines strong radiative recombination continua (RRC) emission, with inter-orbit variability providing a recombination timescale and corresponding mean particle density to allow scaling of this lower ionisation flow component.

In Section 6 we outline a self-consistent physical picture of a highly ionised, high speed wind, which shocks with the ISM at a sufficiently small radius for strong Compton cooling in the AGN radiation field to result in most of the mechanical energy in the flow being lost. The subsequent radial structure of the decelerating post-shock flow is determined by the competing cooling processes, which provide a physical basis on which to understand the complex X-ray absorption and emission spectra in the 2009 *XMM-Newton* observation of NGC 4051.

**Table 1.** *XMM-Newton* 2009 observation summary. The columns list (1) orbit number, (2) spacecraft revolution number, (3) observation start date and time, (4) observation end date and time

orbit no.	XMM rev. no.	Observation start	Observation end
1	1721	05-03 10:22	05-03 23:04
2	1722	05-05 10:16	05-05 22:57
3	1724	05-09 10:02	05-09 22:41
4	1725	05-11 09:55	05-11 22:32
5	1727	05-15 12:36	05-15 21:40
6	1728	05-17 09:35	05-17 21:22
7	1729	05-19 09:29	05-19 21:06
8	1730	05-21 09:22	05-21 21:01
9	1733	05-27 09:02	05-27 21:31
10	1734	05-29 09:09	05-29 21:18
11	1736	06-02 08:43	06-02 21:12
12	1737	06-04 09:55	06-04 20:58
13	1739	06-08 08:34	06-08 20:40
14	1740	06-10 08:16	06-10 20:37
15	1743	06-16 08:23	06-16 20:15

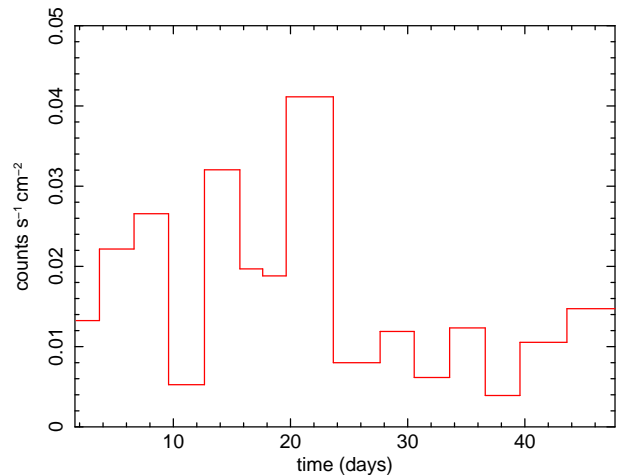


**Figure 1.** Mean RGS flux levels for the 15 *XMM-Newton* orbits of the 2009 observing programme. The time axis is in MJD-54952

## 2 OBSERVATIONS

NGC 4051 was observed by *XMM-Newton* on 15 orbits between 2009 May 3 and June 15, yielding a total on-target exposure of  $\sim 650$  ks. The present paper uses data from the Reflection Grating Spectrometers, RGS 1 and RGS 2 (den Herder et al. 2001) and the EPIC pn camera (Strüder et al. 2001). Detailed X-ray light curves are given in Alston et al. (2013) while mean RGS flux levels for each satellite orbit are shown in figure 1. Table 1 identifies the spacecraft revolution and respective orbit number, with corresponding observation start and end times. The overall observation was characterised by a generally high soft X-ray continuum over the first half (apart from orbit 4) with four successive high flux orbits (5-8), followed by lower mean continuum levels from orbit 9 onward.

### 3 MODELLING THE OUTFLOW WITH XSTAR

To quantify the overall photoionised absorption in the complex outflow in NGC 4051 the RGS and EPIC spectra for the sum of the 4 high flux orbits 5-8 were modelled in Xspec (Arnaud 1996) with alternative grids based on the XSTAR photoionisation code (Kallman et al. 1996).

#### 3.1 RGS data

For the RGS data, where most absorption lines appear intrinsically narrow, we chose grid 18 from the XSTAR library, which includes a fixed turbulent velocity of  $100 \text{ km s}^{-1}$  to minimise computing time. Grid 18 covers an ionisation parameter range in  $\log \xi$  from  $-4$  to  $+4 \text{ erg cm s}^{-1}$ , and column densities from  $10^{19}$  to  $10^{23} \text{ cm}^{-2}$ . Abundances of relevant metals from C to Fe were initially set to solar values, but allowed to vary in the final spectral fitting.

The composite high-flux RGS spectrum was first fitted by a power law plus black body to provide a smooth match to the continuum. Positive Gaussians (determined from fitting the sum of the low flux spectra of orbits 4,11,13) were then added to the continuum to represent the main BEL and the strong FeXVII emission lines near  $17 \text{ \AA}$ . A number of *redge* components were added to represent the stronger RRC, with the normalisation of each left free to vary. Finally, guided by the intriguing observation that very few absorption lines in the RGS spectra appear to penetrate below  $\sim 50\%$  of the continuum, an unabsorbed fraction of the power law plus black body continuum was included in the model.

A sequence of photoionised absorbers from grid 18 was then added to achieve the best statistical fit over the whole  $6\text{-}36 \text{ \AA}$  RGS waveband. The ionisation parameter, column density and velocity (output as a modified redshift) were the primary free parameters of each absorber. In the event the recorded modelling was limited to the  $10\text{-}36 \text{ \AA}$  waveband due to the low RGS sensitivity at shorter wavelengths.

An initial fit to the RGS 1 data over the waveband  $17\text{-}24 \text{ \AA}$ , dominated by absorption lines of OIV, V, VI, VII and VIII and largely independent of relative abundances, required two photoionised components, expressing the strong low ( $\sim 500 \text{ km s}^{-1}$ ) and higher ( $\sim 4000 \text{ km s}^{-1}$ ) velocity absorption in OVII and OVIII. The fit was then extended to  $36 \text{ \AA}$ , to include the resonance lines of NVII, NVI and CVI, and with both RGS1 and RGS2 data, and finally over the waveband  $10\text{-}36 \text{ \AA}$ , covering the higher energy K-shell resonance transitions of Ne, and a potential complex of Fe-L lines. For the full band fits the abundances were allowed to vary, although being tied for the same element across the separate ionised components.

A total of 7 photoionised absorbers yielded significant incremental improvements to the  $10\text{-}36 \text{ \AA}$  fit, with an overall reduction from  $\chi^2/\text{d.o.f.} = 6785/4125$  to  $\chi^2/\text{d.o.f.} = 5048/4094$ . Intriguingly, a further significant reduction to  $\chi^2/\text{d.o.f.} = 4996/4093$  was found with  $28 \pm 5 \%$  of the continuum unabsorbed. The parameters of this multi-absorber fit (illustrated in figure 2) are listed in Table 2.

The abundances of the more important elements in the best fit were C:  $0.29 \pm 0.16$ , N:  $0.62 \pm 0.35$ , O:  $0.68 \pm 0.34$ , Ne:  $0.41 \pm 0.30$  and Fe:  $1.9 \pm 1.1$ . While these values are noted,

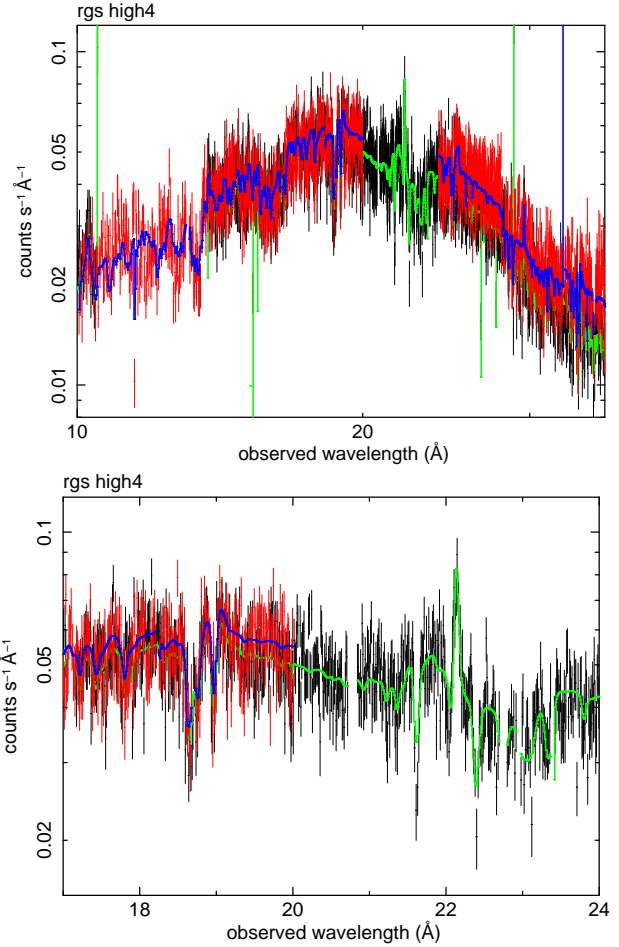


**Figure 2.** XSTAR model fit to the combined RGS1 and RGS2 spectra summed over the four high-flux orbits 5-8 is shown for the full  $10\text{-}36 \text{ \AA}$  waveband in the upper panel, with the section covering strong absorption in oxygen highlighted in the lower panel

only the over-abundance of Fe made a substantial difference to the fit parameters.

Components 1, 2 and 7 represent the high velocity absorption observed most strongly in the soft X-ray data in OVIII and NeX, and it is notable that they pick out similar velocities to the values obtained from Gaussian fits to the absorption in OVIII, NVII and CVI Lyman- $\alpha$  (Paper I). Component 7 is the least significant, with a lower column density indicating a minor constituent at the highest post-shock velocities.

Components 3 and 4 represent the lower velocity/lower ionisation absorption, observed particularly strongly in absorption lines of OV, OVI and OVII and the Fe UTA at  $\sim 15\text{-}16.5 \text{ \AA}$ . The absence of an intermediate velocity component is consistent with the absorption velocity profiles in Paper I, showing with a relative lack of absorption between  $\sim 3000$  and  $\sim 1000 \text{ km s}^{-1}$ .

Component 5 represents the low velocity absorption seen across a wide range of ionisation parameter, interpreted in Paper II as self-absorption in the BEL, where a high-inclination to the line of sight constrains the projected flow velocities.

Component 6 was a surprise, but is strongly required by the fit. Although only hinted in individual spectra, the

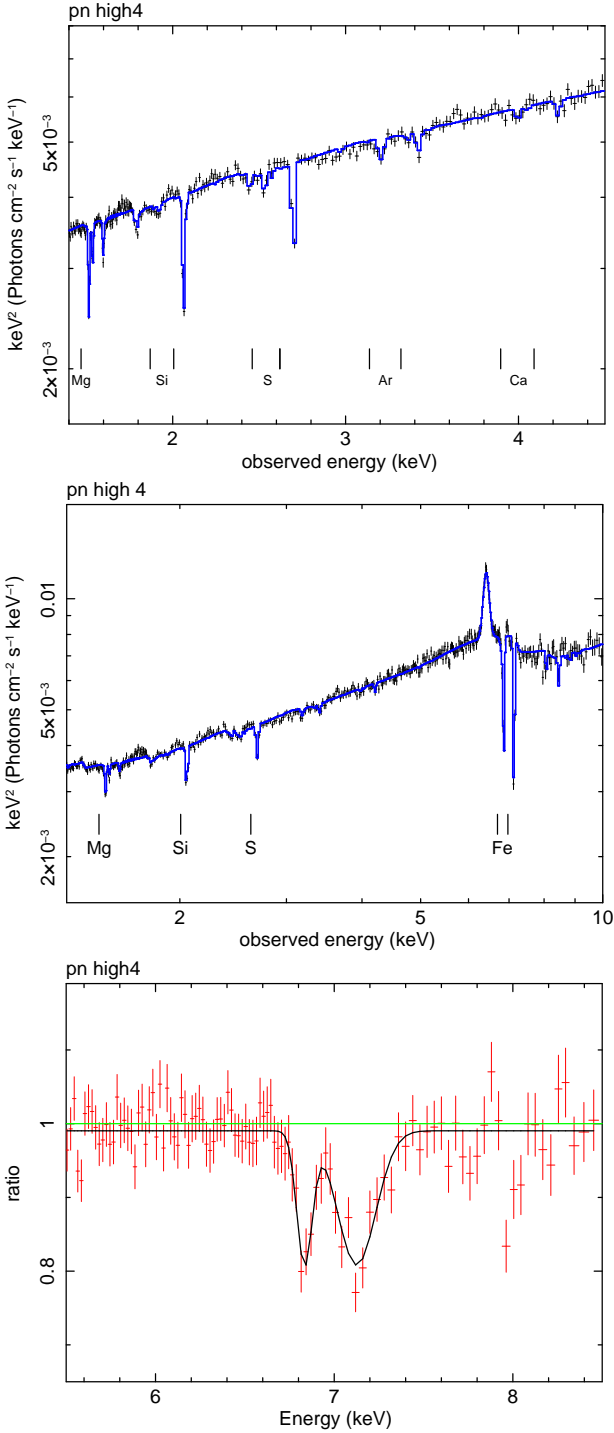


**Figure 3.** XSTAR model fits to the combined pn spectra over the four high flux orbits 5-8. The top panel is restricted to the 1.3-5 keV energy band covering the K-shell resonance lines of Mg, Si, S, Ar and Ca. The mid panel shows a second fit extended to include the strong Fe K absorption lines. The lower panel reproduces a simple Gaussian fit to the Fe K spectral lines, with a broad Lyman- $\alpha$  line indicative of a spread of outflow velocities

**Table 2.** Parameters of the photoionised outflow fitted to the RGS data. Column density is in H atoms  $\text{cm}^{-2}$  and ionisation parameter in  $\text{erg cm s}^{-1}$

Comp	$\log\xi$	$N_H$	velocity ( $\text{km s}^{-1}$ )	$\Delta\chi^2$
1	$3.0\pm 0.1$	$4.3\pm 0.4\times 10^{22}$	$-5760\pm 500$	488/3
2	$2.5\pm 0.1$	$1.0\pm 0.1\times 10^{22}$	$-3720\pm 300$	113/3
3	$1.6\pm 0.2$	$7\pm 0.3\times 10^{20}$	$-510\pm 150$	94/3
4	$0.8\pm 0.1$	$1.6\pm 0.3\times 10^{21}$	$-120\pm 45$	797/3
5	$2.6\pm 0.2$	$2\pm 0.5\times 10^{21}$	$-630\pm 350$	174/3
6	$-0.82\pm 0.1$	$4\pm 1.5\times 10^{20}$	$+360\pm 60$	48/3
7	$3.2\pm 0.2$	$1\pm 0.3\times 10^{21}$	$-10290\pm 1000$	23/3

requirement of a red-shifted absorption component at low velocity is interesting as a possible indicator of post-shock matter falling back from the contact discontinuity, having slowed to below the local escape velocity. The absence of a similar red-shifted absorber in the comparable analyses of Steenbrugge et al. (2009) and Lobban et al. (2011) would argue against an alternative origin in a high velocity cloud in the line of sight in the host galaxy, as reported for Mkn 509 (Ebrero et al. 2011).

The outflow velocity and ionisation parameter of components 1-5 and 7 are plotted in figure 4, together with the main absorbing ions located at the ionisation parameter of maximum abundance for a gas in equilibrium.

### 3.2 EPIC data

Fitting the EPIC pn absorption spectra, again for the sum of the 4 high flux orbits (5-8), allows an extension of the XSTAR modelling to heavier ions whose K-shell wavelengths fall outside the sensitive range of the RGS. The generally higher velocities and ionisation levels seen in the EPIC spectrum led to a preference of grid 21 for XSTAR modelling, with a higher turbulent velocity of  $1000 \text{ km s}^{-1}$ , but otherwise a similar parameter range to grid 18. The continuum was first modelled by a partially covered power law plus reflection, the model *pcref* described in detail in Paper III. Positive Gaussians were added to represent the Fe K fluorescence line at  $\sim 6.4 \text{ keV}$  and an apparent red wing.

Initially restricting the fit to the 1.3-5 keV band, covering the K-shell resonance lines of Mg, Si, S, Ar and Ca, the continuum model yielded a moderately good fit ( $\chi^2 = 888/738$ ). However, several absorption lines were clearly evident in the data:model ratio plot. The addition of a single XSTAR component of grid 21 matched the stronger of these features and provided an excellent overall fit ( $\chi^2 = 743/735$ ), with ionisation parameter  $\log\xi = 3.2\pm 0.1$  and column density  $1.8\pm 0.2\times 10^{22} \text{ cm}^{-2}$  (figure 3, top panel). The relative blue-shift of this more highly ionised component,  $2.8\pm 0.2\times 10^{-2}$ , corresponds to an outflow velocity of  $9100\pm 600 \text{ km s}^{-1}$ , consistent with the strongest high velocity component found in NeX Lyman- $\alpha$  absorption in the RGS data (Paper I).

Extending the EPIC spectral fit to 10 keV includes the strong Fe K absorption lines. The continuum was again modelled with *pcref*, but provided a poor fit ( $\chi^2 = 1829/1358$ ) with strong negative residuals near 7 keV. The addition of photoionised absorption with grid 21 produced a very substantial improvement ( $\chi^2 = 1445/1362$ ), due mainly to matching the resonance absorption lines of Fe XXV

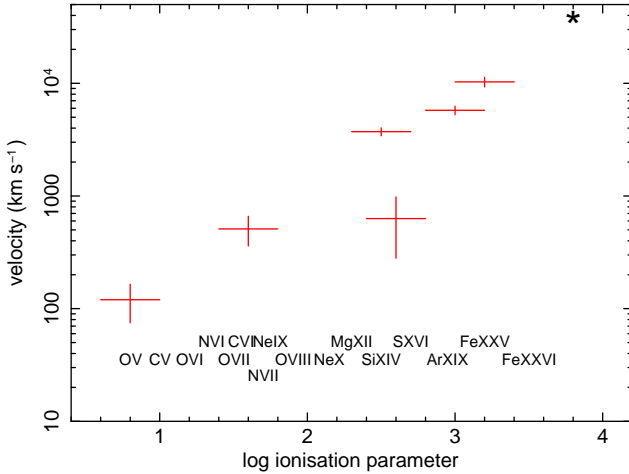


**Figure 4.** Outflow velocity and ionisation parameter for each of the XSTAR photoionised absorbers derived from fitting to the RGS spectra, together with a high point representative of the pre-shock wind. The main trend is consistent with the linear correlation of velocity and ionisation parameter expected for a mass-conserved cooling flow

and Fe XXVI (figure 3, mid panel). The XSTAR fit over this wider energy band had a similar ionisation parameter ( $\log\xi=3.4\pm0.1$ ) and column density ( $3.9\pm0.7\times10^{22}\text{cm}^{-2}$ ), but a lower velocity ( $7600\pm500\text{km s}^{-1}$ ). A probable explanation for this difference, which appears to go against the general velocity-ionisation trend, is that the Fe K absorption lines are so strong as to dominate the fit, while the Fe Lyman- $\alpha$  absorption line appears unusually broad in the data and may not be well modelled with a single velocity. The lower panel of figure 3 illustrates the relevant structure of the Fe K absorption, where the ratio of data to continuum is modelled by Gaussians. It appears likely that the XSTAR fit is finding a mean value in a velocity range from  $\sim 5000$  -  $9000\text{km s}^{-1}$ , perhaps tracing the post-shock flow across the main Compton cooling shell. In that context,  $\sim 5000\text{km s}^{-1}$  may then indicate the point where 2-body cooling becomes important as the temperature falls below  $\sim 1\text{keV}$  (Section 6 and Appendix), and the highly ionised flow changes rapidly to a low ionisation flow.

In summary, XSTAR modelling finds the RGS and EPIC absorption parameters are in good agreement in the high ionisation/high velocity region of overlap. The linear trend of velocity and ionisation parameter is clearly seen in figure 4, as expected for a cooling post-shock flow. The weak high velocity component in the RGS data may indicate density structure in the post shock flow.

Finally, a 7th point is added to figure 4 to represent the pre-shock wind, with velocity  $v\sim 0.12c$  (Paper III) and an ionisation parameter of  $\log\xi=3.8$ , the latter assuming the factor of 4 increase in density (along with a similar decrease in velocity) expected across a strong shock.

An outstanding question for the mass-conserved shocked flow interpretation is raised by the strong column density gradient between the high and lower ionisation XSTAR components. We interpret this in Section 6 in terms of the onset of additional two-body cooling, causing the flow to pass quickly through intermediate velocity and ionisation stages.

#### 4 VARIABLE FE K ABSORPTION AND THE HIGHLY IONISED FLOW COMPONENT

The strongest absorption lines in the EPIC spectrum are generally those of the resonance transitions of FeXXV 1s-2p and FeXXVI Lyman- $\alpha$  (figure 3, mid panel). The ratio of line depths is a sensitive measure of ionisation state, and a detailed examination of the Fe K absorption profile in Paper III showed that the line ratio - and implicitly the ionisation - could change significantly between adjacent orbits.

Figure 5 compares the Fe K absorption profile for orbits 6 and 7 (where similar spectra have been co-added for greater clarity) with that for orbit 8 where the ionising flux  $\gtrsim 7.1\text{keV}$  has increased by a factor of  $\sim 2$ , to the highest level of the 2009 campaign. While the two absorption lines are of similar depth in the first case, the  $7.1\text{keV}$  Fe XXVI Lyman- $\alpha$  line is significantly the stronger in orbit 8, indicating the ionisation state of the highly ionised flow component has changed on a timescale of  $\sim 2$  days (table 1).

For an ionisation front moving into a low density medium, as here, the observed response time will be governed by the recombination time. Assuming a post-shock temperature for the more highly ionised flow of  $\sim 1\text{keV}$  (Paper I), and a recombination coefficient of  $\sim 5\times 10^{-12}\text{cm}^3\text{s}^{-1}$  (Verner and Ferland 1996), the observed variability timescale corresponds to an electron density of  $\sim 4\times 10^6\text{cm}^{-3}$ .

Comparing this measure of the particle density of the highly ionised flow with the corresponding column density from XSTAR modelling,  $N_H\sim 4\times 10^{22}\text{cm}^{-2}$ , yields a primary cooling shell thickness of  $\sim 10^{16}\text{cm}$ . We use this value in Section 6 to estimate the shock radius.

#### 5 RECOMBINATION CONTINUA FROM THE LOWER IONISATION FLOW

Paper II reported a significant emission component from the NVII RRC (threshold wavelength  $18.59\text{\AA}$ ), though evidence for inter-orbit variability is affected by blending with high velocity absorption in OVIII Lyman- $\alpha$  ( $18.968\text{\AA}$ ). The NVI RRC is strongly blended with OVII absorption, while the OVII RRC sits at the upper wavelength edge of a strong Fe UTA. Fortunately, both CV and CVI RRC lie in spectral regions relatively free from absorption lines. Velocity profiles of both carbon RRC for a composite of all 15 orbits are of a similar form, with distinct - though not identical variability - between individual orbits and groups of orbits with similar continuum levels. The 15-orbit sum and a representative set of emission profiles for CVI are shown in figure 6.

Figure 6 (top left panel) shows the composite velocity profile for the whole 2009 observation of NGC 4051, with zero velocity at the threshold wavelength of the CVI RRC ( $25.303\text{\AA}$ ). The statistical quality of the composite data, plotted at high velocity resolution ( $300\text{km s}^{-1}$ ), allows non-RRC features to be resolved and identified. To the blue side they include the low velocity absorption component of NVI 1s-3p (seen near  $-5000\text{km s}^{-1}$ ) and multiple NVII Lyman- $\alpha$  absorption components (near  $-7000$ ,  $-10000$  and  $-12500\text{km s}^{-1}$  in the plot). Positive and negative spikes at  $\sim 8200$  and  $\sim 5000\text{km s}^{-1}$  are due to a dead pixel and a chip gap in the RGS CCDs.

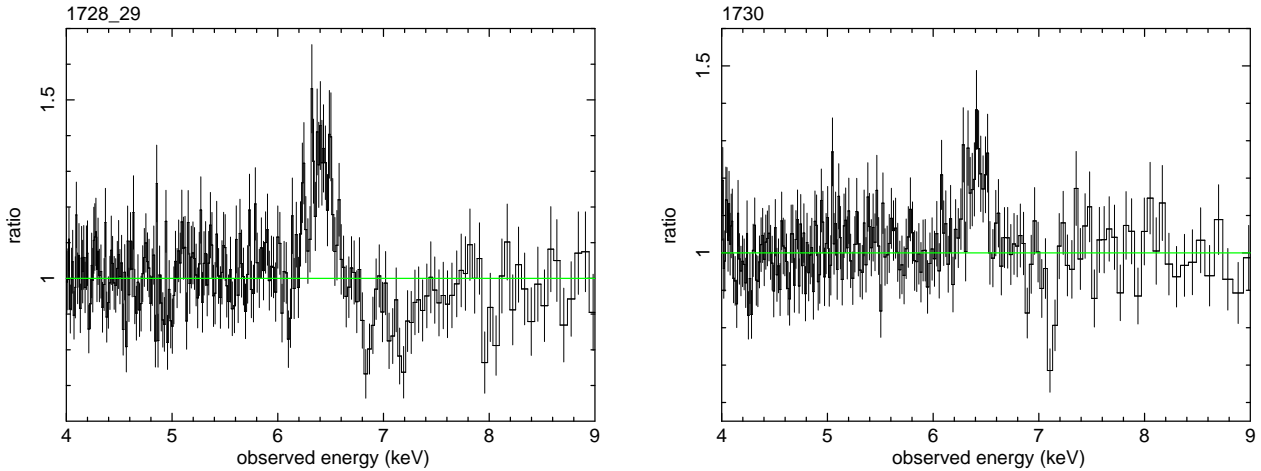


**Figure 5.** Variable absorption profiles for the composite of orbits 6 and 7 and for the peak flux orbit 8, indicating an increase in ionisation with higher continuum flux

The composite 15-orbit RRC emission profile is quite unlike the saw-tooth shape expected for stationary matter, and extends blue-ward of the zero velocity threshold by  $\sim 4000 \text{ km s}^{-1}$ . While some part of the RRC width will be a measure of the electron temperature in the recombining gas, the shape of the composite profile indicates a mean outflow velocity of  $\sim 2000 \text{ km s}^{-1}$ , similar to the velocity gap at  $\sim 1500\text{--}3500 \text{ km s}^{-1}$  in the absorption profiles in the C, N and O Lyman- $\alpha$  lines (Paper I), and interpreted in Section 6 as a consequence of a rapidly increased cooling rate.

The middle and lower left panels of figure 6 show the same CVI RRC profile for a composite of the early orbits 1-3 and for orbit 4, when the mean continuum level has fallen (figure 1) by a factor  $\sim 4$ . The CVI RRC is of similar strength in both plots, setting a lower limit to the relevant recombination time of  $\sim 2$  days (table 1).

The right hand side of figure 6 continues the orbital sequence with the upper panel being a composite profile from the high flux orbits 5-8, with the peak emission shifted still more strongly to the blue. In contrast, the high velocity RRC component has essentially disappeared by orbit 9 (right side, mid panel), with an integrated flux lower than for orbits 5-8 by a factor  $4.5 \pm 1$ .

Reference to the orbit timing data in table 1 shows an interval of  $\sim 6$  days between orbits 8 and 9, providing a firm upper limit to the recombination time for the relevant flow component  $\leq 5.5$  days. However, additional Swift and RXTE monitoring (Alston et al. 2013) shows a high continuum flux midway between orbits 8 and 9, further constraining the RRC decay time to  $\leq 2.5$  days. We assume below a recombination time of 2 days.

Assuming an electron temperature from the mean RRC profile of  $\sim 4\text{eV}$ , a CVI recombination coefficient of  $\sim 10^{-11} \text{ cm}^3 \text{ s}^{-1}$  (Verner and Ferland 1996) and the observed RRC decay time indicate a density of  $\sim 3 \times 10^6 \text{ cm}^{-3}$ . The related column density of  $\sim 10^{21} \text{ cm}^{-2}$  from XSTAR modelling then translates to an absorbing path length of  $3 \times 10^{14} \text{ cm}$  for the lower ionisation flow component.

Variability in the RRC contrasts with the lack of variability in the BEL of the same ions. The probable explanation lies in the higher blue shift of the RRC emission and

a shorter light travel time. Since a substantial RRC flux implies a wide angle flow, a delayed response to a lower continuum will be a product of light travel time and intrinsic recombination timescale, with the more blue-shifted emission from matter observed at a smaller offset angle.

A similar examination of the emission profiles of the CV RRC supports this conclusion, with the 15-orbit composite showing a clearer separation into two velocity components. While the higher velocity component varies in a similar way to CVI, the low velocity component in CV appears to vary little with overall flux level, similar to the BEL.

## 6 DISCUSSION

Modelling the RGS and EPIC pn absorption spectra from the 2009 *XMM-Newton* observation of NGC 4051 confirms a general correlation of outflow velocity and ionisation, consistent with mass conservation in a cooling shocked wind (King 2010, Paper I), while also quantifying the strong gradient in column density with ionisation level. Inter-orbit changes in the ratio of FeXXV and FeXXVI absorption lines allow an estimate of the mean particle density in the highly ionised post-shock flow, with similarly rapid variability in strong RRC emission constraining the density in the lower ionisation flow. In this Section we outline a model incorporating the above data, while providing a physical basis for identifying a fast ionised wind and a ‘warm absorber’ as early and late stages in a continuous, mass-conserved flow.

Figure 7 illustrates the envisaged scenario, assuming spherical symmetry and a uniform radial flow. The highly ionised wind collides with the ISM sufficiently close to the AGN for strong Compton cooling of the shocked gas to define a shell where the ionisation level remains sufficiently high for ionised Fe K absorption. At a critical juncture along the flow, 2-body processes become important (see Appendix) and the flow cools more rapidly over a narrower region, where X-ray absorption (and emission) is dominated by the lighter metals (O,N,C).

For the highly ionised flow, a density estimate from observed variability in the Fe K absorption line ratio (Section

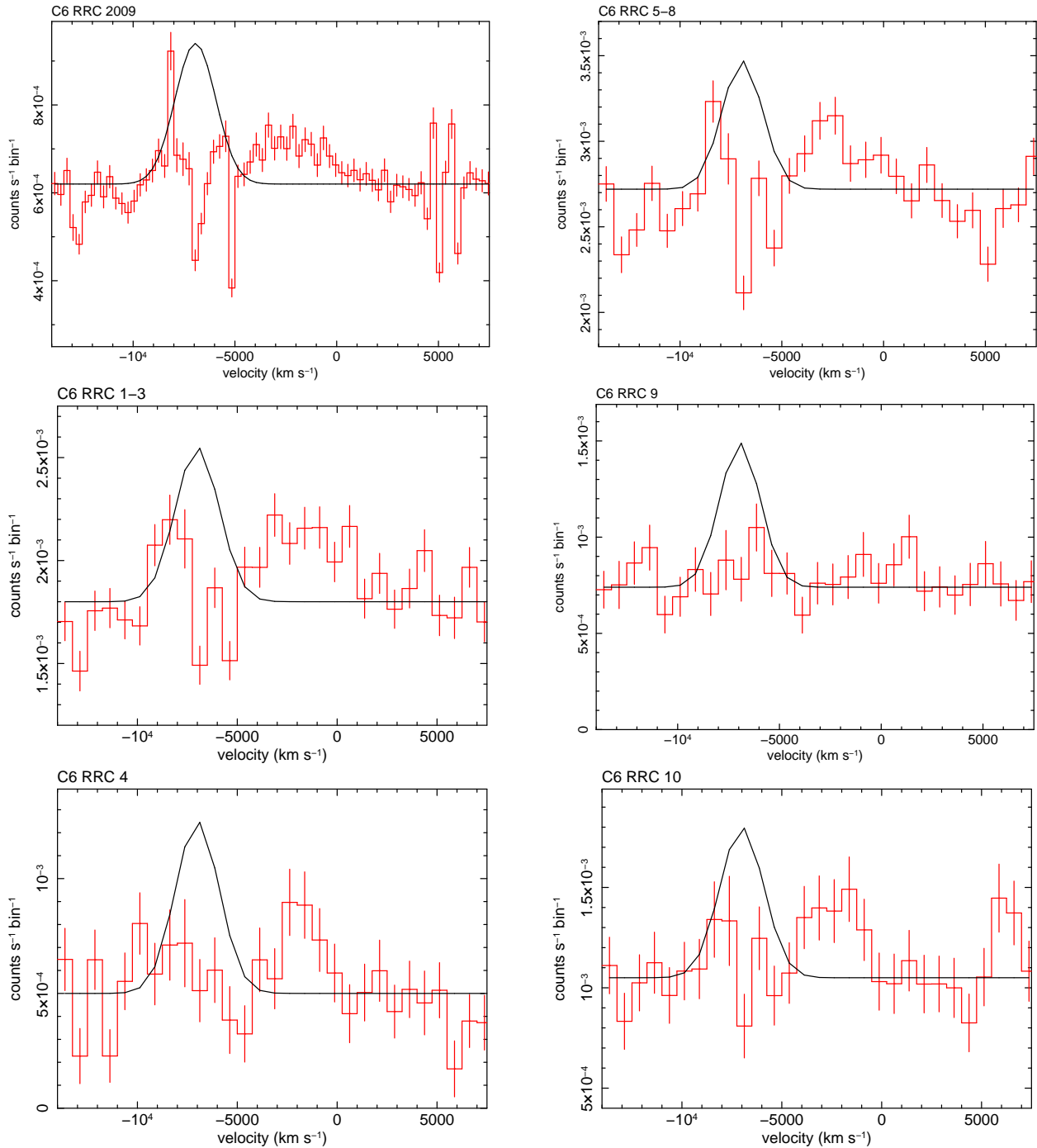


**Figure 6.** (left panel, from top) Composite velocity profile of the CVI RRC summed over the full 2009 observation. A strong RRC is visible, extending blue-ward by  $\sim 4000$  km s $^{-1}$  from the rest frame threshold. The sharp spikes at  $-8200$  and  $\sim 5000$  km s $^{-1}$  are due to a chip gap and dead pixels in the RGS CCDs, while the absorption and emission structure beyond  $-4500$  km s $^{-1}$  is identified with low velocity absorption in the NVI K- $\beta$  line and the BEL and both low and higher velocity absorption in NVII Lyman- $\alpha$ . The mid and lower panels show the same profile, with velocity resolution degraded from 300 to 750 km s $^{-1}$ , for orbits 1-3 and 4, respectively. (right panel, from top) Composite velocity profile of the CVI RRC with velocity resolution of 750 km s $^{-1}$ , for orbits 5-8, 9, and 10. Note different y-axis scaling and see text for discussion.

4), and an absorption column from the XSTAR modelling indicate an absorption length of  $\sim 10^{16}$  cm. Comparison with the theoretical Compton cooling time for NGC 4051 of  $\sim 600$  R $^2$  yr (from Appendix, equ.2, with  $M=1.7 \times 10^6 M_{\odot}$ ), and assuming a mean velocity for the highly ionised flow of 6000

km s $^{-1}$ , finds the observed cooling length to correspond to a shock at a radial distance  $R \sim 0.03$  pc ( $\sim 10^{17}$  cm) from the black hole.

Repeated variability in the CVI RRC flux (Section 5) indicates a recombination time for the lower ionisation mat-

ter of  $\sim 2$  days. Together with a related column density from XSTAR modelling, this indicates an effective absorbing path length of  $4 \times 10^{14}$  cm for the lower ionisation flow component.

Given these estimates of shell radius and thickness, the RRC emission measure provides an overall consistency check on the above scaling. A CVI RRC flux from the spectral fit to orbits 5 - 8 of  $\sim 10^{-4}$  photons  $\text{cm}^{-2}\text{s}^{-1}$  and recombination rate of  $10^{-11}$   $\text{cm}^3 \text{s}^{-1}$ , assuming 30 percent of recombinations direct to the ground state, corresponds to an emission measure of  $\sim 4 \times 10^{63} \text{cm}^{-3}$ , for a Tully-Fisher distance to NGC 4051 of 15.2 Mpc.

For a mean density of  $\sim 3 \times 10^6 \text{cm}^{-3}$ , the emission volume ( $4\pi R^2 \Delta R$ ) is then  $\sim 10^{50} \text{cm}^3$ . With the derived values of recombining shell thickness  $\delta R \sim 3 \times 10^{14} \text{cm}$ , and shell radius  $R \sim 10^{17} \text{cm}$ , we find the measured RRC flux is reproduced within a factor 2. Given the approximate nature and essential averaging of many observed and modelled parameters, the self-consistency check is remarkably good.

Finally, we note that all momentum-driven outflows in AGN will ultimately stall (King 2003, 2010), while the measured column densities in UFOs show they must be variable on relatively short timescales (King 2010a). The repeated shocks will leave behind heated and compressed gas (both wind and ISM), which can linger for some time before dispersing or falling back towards the black hole (note: the escape velocity for NGC 4051 at  $R \sim 10^{17} \text{cm}$  is  $\sim 500 \text{km s}^{-1}$ ).

We suggest that this matter, observed here as the low velocity/low ionisation component, may form much of the warm absorber frequently observed in AGN (Tombesi et al. 2013). The low ionisation, red-shifted absorption component indicated in our XSTAR modelling offers an intriguing prospect of tracking the circulation of the stalled wind and the ISM that has been progressively removed from smaller radii.

## 7 SUMMARY

Combining the analysis of emission and absorption spectra with XSTAR modelling provides a picture of the overall NGC 4051 outflow consistent with a fast primary wind being shocked at a radial distance of order  $10^{17} \text{cm}$ , well within the zone of influence of a supermassive black hole of mass  $1.7 \times 10^6 M_{\odot}$ . While the analysis necessarily involves substantial simplifications, with a few discrete components providing a coarse description of a quasi-continuous and rapidly evolving flow, the resulting picture appears robust and physically attractive.

The shocked gas initially cools in the strong radiation field of the AGN, with a Compton cooling length essentially determining the absorption columns of Fe and the other heavy metal ions. Two-body processes provide additional cooling as the density rises down-stream, rapidly becoming dominant. Absorption (and emission) in the soft X-ray band then maps this thinner, outer region of the post-shock flow ahead of the contact discontinuity.

The inclusion of an unabsorbed continuum in the best-fit XSTAR model may be evidence for denser cooling clumps in the flow (figure 7). Although our analysis has assumed a uniform radial flow, any density variations at the shock will be enhanced by differential cooling. Cooling radiation

from the flow may also contribute significantly to a partially covered soft X-ray continuum.

We note that shocking with the ISM or other matter in the vicinity of the AGN, as found for NGC 4051, may provide the link between ultra-fast outflows (Tombesi et al. 2010) and the equally common ‘warm absorbers’ in such objects. In that scenario the onset of strong 2-body cooling would result in the intermediate column densities being relatively small and difficult to see with less sensitive observations than in the present case.

An important consequence of powerful AGN winds losing much of their energy by radiative cooling after shocking against the surrounding gas is that feedback from such winds will be momentum-driven, consistent with the observed form of the observed  $M-\sigma$  relation (King 2003).

## ACKNOWLEDGEMENTS

The work reported here is based on observations obtained with *XMM-Newton*, an ESA science mission with instruments and contributions directly funded by ESA Member States and the USA (NASA). Simon Vaughan was PI of the 2009 observation of NGC 4051. We thank the anonymous referee for encouraging greater clarity in the text.

## REFERENCES

- Alston W.N., Vaughan S., Uttley P. 2013, MNRAS, 429, 75  
 Arnaud K.A. 1996, ASP Conf. Series, 101, p. 17, Astron. Data Analysis, eds G.H.Jacoby and J.Barnes, Astron. Soc. Pacific  
 Collinge M.J. et al. 2001, ApJ, 557, 2  
 Costantini E. et al. 2007 A&A, 461, 121  
 den Herder J.W. et al. 2001, A&A, 365, L7  
 Ebrero J. et al. 2011, A&A, 534, 40  
 Kaastra J.S. et al. 2002, A&A, 386, 427  
 Kallman T., Liedahl D., Osterheld A., Goldstein W., Kahn S. 1996, ApJ, 465, 994  
 King A.R. 2003, ApJ, 596, L27  
 King A.R. 2005, ApJ, 635, L121  
 King A.R. 2010, MNRAS, 402, 1516  
 King A.R. 2010a, MNRAS, 408, L95  
 King A.R., Zubovas K., Power C., 2011, MNRAS, 415, L6  
 Lobban A., et al. 2011, MNRAS, 414, 1965  
 Ogle P.M., Mason K.O., Page M.J., Salvi N.J., Cordova F.A., McHardy I.M., Priedhorsky W.C. 2004, ApJ, 606, 151  
 Pounds K.A., Reeves J.N., King A.R., Page K.L. 2004, MNRAS, 350, 10  
 Pounds K.A., Vaughan S. 2011, MNRAS, 413, 1251 (Paper I)  
 Pounds K.A., Vaughan S. 2011a, MNRAS, 415, 2379 (Paper II)  
 Pounds K.A., Vaughan S. 2012, MNRAS, 423, 165 (Paper III)  
 Smith R.A.N., Page M.J., Branduardi-Raymont G., 2007, A&A, 461, 135  
 Steenbrugge K.C, Fenovcik M., Kaastra J.S., Costantini E., Verbunt F. 2009, A&A, 496, 107  
 Strüder L. et al. 2001, A&A, 365, L18  
 Tombesi F., Cappi M., Reeves J.N., Palumbo G.C., Yaqoob T., Braito V., Dadina M. 2010, A&A, 521, A57  
 Tombesi F., Cappi M., Reeves J.N., Nemmen R.S., Braito V., Gaspari M., Reynolds C.S. 2013, MNRAS, 430, 1102  
 Verner D.A. and Ferland G.J. 1996, ApJS, 103, 467  
 Zubovas K. and King A.R. 2012, ASPC, 460, 235

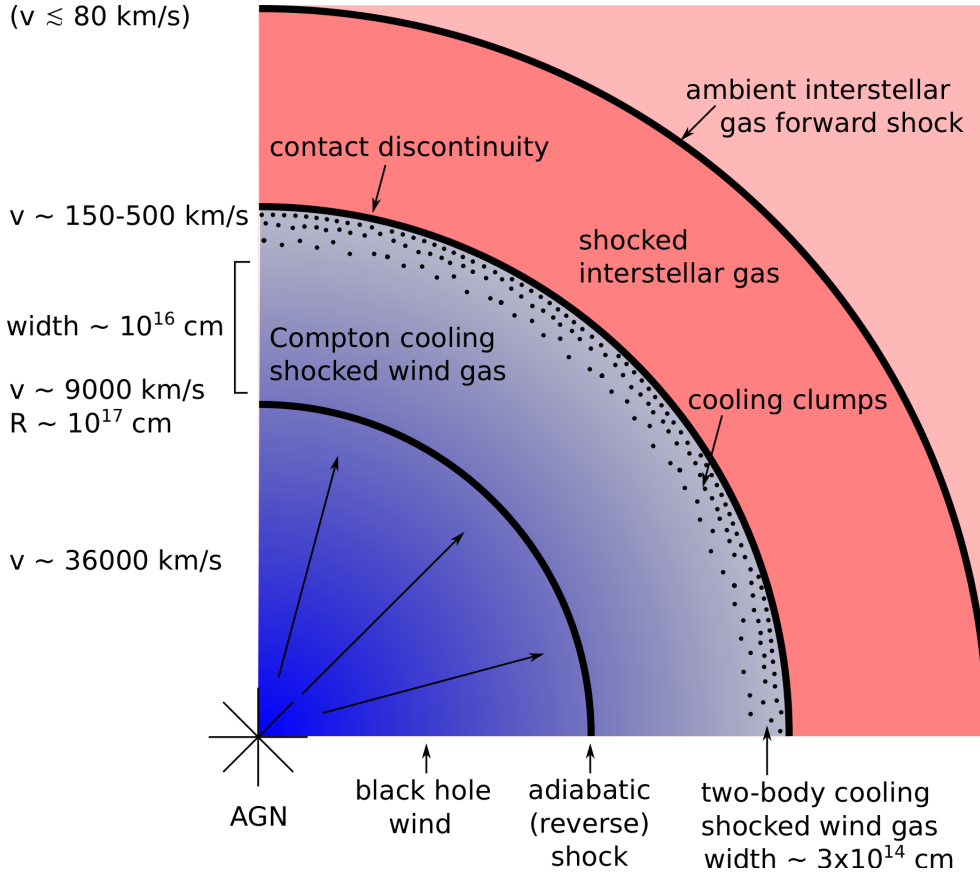


**Figure 7.** Structure of the NGC 4051 outflow, not to scale, showing a highly ionised wind colliding with the ISM at a radius  $\sim 10^{17}$  cm, the strong shock causing a sudden factor 4 drop in velocity. Strong Compton cooling of the shocked gas defines a thin shell where the velocity continues to fall but the ionisation state remains sufficiently high for strong Fe K absorption. Further along, when 2-body processes become important, the flow cools more rapidly and slows over a narrower region where absorption (and emission) are dominated by the lighter metals seen in the soft X-ray spectrum. Although not used in the analysis, density variations in the shocked gas will be enhanced later in the flow and are pictured as cooling clumps

## 8 APPENDIX

Immediately after the (adiabatic) shock, slowing the fast wind from  $v \sim 0.12c$  to  $1/4$  of this speed, the free-free and Compton cooling times are

$$t_{\text{ff}} \cong 3 \times 10^{11} \frac{T^{1/2}}{N} \text{ s} = 2 \frac{R_{16}^2}{M_8 \dot{m}} \text{ yr} \quad (1)$$

and

$$t_{\text{C}} = 10^{-4} \frac{R_{16}^2}{M_8} \text{ yr} \quad (2)$$

respectively (see King, Zubovas & Power, 2011: here  $T, N$  are the postshock temperature and number density,  $R_{16}$  is the shock radius in units of  $10^{16}$  cm,  $M_8$  is the black hole mass in units of  $10^8 M_{\odot}$ , and  $\dot{m} \sim 1$  is the Eddington factor of the mass outflow rate).

After the adiabatic shock, the gas cools rapidly from  $T \sim 1.6 \times 10^{10}$  K by inverse Compton cooling, while its density rises as  $N \propto T^{-1}$  (isothermal shock – pressure almost constant). So

$$t_{\text{ff}} \propto \frac{T^{1/2}}{N} \propto T^{3/2}, \quad (3)$$

which means that the free-free cooling time decreases sharply while the Compton time does not change. When  $T$  has decreased enough below the original shock temperature, free-free (and all the other atomic two-body processes) becomes faster than Compton.

From (1, 2) above this requires

$$\left(\frac{T}{T_s}\right)^{3/2} < 5 \times 10^{-5} \quad (4)$$

or

$$T < 2 \times 10^7 \text{ K} \quad (5)$$

showing the temperature of ionisation species forming around a few keV is determined by atomic cooling processes rather than Compton cooling. As the temperature falls further, two-body cooling becomes dominant, with the subsequent flow cooling still more rapidly and both velocity and ionisation level falling quickly. This strong cooling phase is traced in the present observation by absorption and emission in the lighter metals (C, N, O) through increasingly narrow shells prior to the build up of low velocity/low ionisation matter ahead of the contact discontinuity.